Reconfigurable Inductive Power Transfer Scheme Across Reinforced Concrete Walls for Building Attached Photovoltaic Grid Connection

Peng Gu, *Member, IEEE*, Xingzhen Guo, Yunrui Hao, Xinzhe Wang, *Graduate Student Member, IEEE*, Jiliang Zhang, *Senior Member, IEEE*, Dongsheng Yang, *Senior Member, IEEE*, and Yijie Wang, *Senior Member, IEEE*

***Abstract*—A building attached photovoltaic inductive power transfer (IPT) system is proposed in this article. The coupling coefficient is significantly improved by the designed ferrite bridge (FB), which enables efficient wireless power transfer across building walls. The influence of wall-embedded rebar on system performance is analyzed, and corresponding methods to overcome it are developed. The additional core loss caused by FB and rebar is analyzed. A multitap auto-coupling coil is proposed. The voltage conversion ratio of the system can be reconfigured by switching the taps of the coil. Based on this, an IPT system is proposed to enable wireless connection between the outdoor photovoltaic system and the indoor microgrid. The circuit model of the system is built, and the transmission characteristics of the system and the losses of each part are analyzed. A three-tap IPT system prototype is built to simulate the situation of passing through a 360-mm building wall. Experiments show that the IPT system has an efficiency of approximately 90%.**

***Index Terms*—Building attached photovoltaic (BAPV), ferrite bridge (FB), inductive power transfer (IPT), multitap reconfigurable coupling structure, rebar influence.**

I. Introduction

PHOTOVOLTAIC technology is widely adopted for power generation and increasingly integrated into buildings. Solar energy is converted into electrical energy and used by consumers inside the building. Depending on how photovoltaic panels are installed, photovoltaic systems classified into building attached photovoltaic (BAPV) and building integrated photovoltaic (BIPV). The photovoltaic panels in the BIPV system are building materials, while the photovoltaic panels in the BAPV system are independent of the building. In comparison, the BAPV system is easier to install and is most widely used [1], [2]. The traditional BAPV system relies on cables to connect the photovoltaic modules to the interior of the building, which may lead to various adverse effects. First, cable maintenance within walls is inconvenient and prone to insulation degradation and current leakage. Leaked current can corrode nearby metal structures, posing significant safety hazards [3]. The wall perforation for cable routing can lead to water ingress, thereby shortening the PV system's lifespan [4]. Furthermore, cables may form thermal bridges, which damage the thermal insulation layer in the building and seriously affect the thermal insulation effect [5].

With the rapid advancement of inductive power transfer (IPT) technology, diversified application scenarios have been explored and expanded. Among them, IPT technology has been widely used in electric vehicles [6], autonomous underwater vehicles [7], drones [8], medical devices [9], battery charging [10], wireless lighting [11], etc. Similarly, IPT can be adopted in BAPV systems to achieve wireless power transfer (WPT) through high-frequency, time-varying electromagnetic fields, eliminating the need for physical cables. The coupling coefficient and the quality factor are the two significant factors that limit the power transfer efficiency (PTE) of the IPT system [12]. The coupling coefficient tends to be low in IPT systems with large air gaps. To address this limitation, various innovative magnetic coupling structures were proposed, which can significantly improve the PTE by increasing the coupling coefficient of the system. A square coil with a composite structure was proposed and analyzed to achieve efficient high-power transmission in [13]. A dipole-shaped magnetic coupling structure applied to a meter-range air gap IPT system was proposed and analyzed in [14] and [15]. A cylindrical solenoid coupler (CSC) was proposed in [16] and [17], which significantly improved the coupling coefficient between adjacent coils and extended the effective transmission distance. Ferrite cores made of ceramic materials are commonly used due to

Received 9 February 2025; revised 21 April 2025; accepted 19 May 2025. Date of publication 27 May 2025; date of current version 5 August 2025. This work was supported in part by the National Natural Science Foundation of China under Grant 52307005, in part by China Postdoctoral Science Foundation under Grant 2023TQ0052, in part by Postdoctoral Fellowship Program of China Postdoctoral Science Foundation (CPSF) under Grant GZC20230386, in part by Fundamental Research Funds for the Central Universities under Grant N2404016, and in part by Young Elite Scientist Sponsorship Program by Chinese Society for Electrical Engineering (CSEE) under Grant CSEE-YESS-2023008. Recommended for publication by Associate Editor J. Acero. *(Corresponding authors: Peng Gu; Yunrui Hao.)*

Peng Gu, Xingzhen Guo, Xinzhe Wang, Jiliang Zhang, and Dongsheng Yang are with the College of Information Science and Engineering, Northeastern University, Shenyang 110819, China (e-mail: gupeng@ieee.org; 2470979@stu.neu.edu.cn; wangxinzhe@ieee.org; zhangjiliang1@mail.neu.edu.cn; yangdongsheng@mail.neu.edu.cn).

Yunrui Hao is with Northeastern University, Shenyang 110819, China (e-mail: 2201224@stu.neu.edu.cn).

Yijie Wang is with the School of Electrical Engineering and Automation, Harbin Institute of Technology, Harbin 150001, China (e-mail: wangyijie@hit.edu.cn).

Color versions of one or more figures in this article are available at https://doi.org/10.1109/TPEL.2025.3574008.

Digital Object Identifier 10.1109/TPEL.2025.3574008

their high magnetic permeability. They can guide and constrain magnetic flux, thus enhancing the coupling coefficient. In [18], the coupling under rotational misalignment was improved by inserting ferrite cores into ID-shaped coils for underwater vehicle applications. A cubic magnetic coupling structure was proposed in [19]. By dividing the ferrite core, the coupling coefficient was improved under the same distance-to-diameter ratio. In summary, the coupling coefficient of the IPT system can be significantly improved by designing the ferrite core, thereby improving the PTE of the system.

An innovative building-integrated photovoltaic system with wireless charging function for drones was proposed in [20] and [21]. In this system, drones are wirelessly charged on the building's rooftop using power supplied by photovoltaic panels mounted on the walls. The feasibility of combining WPT system with building photovoltaics is verified. However, the power transfer across the wall is not considered. Also, a compact magnetically integrated coupling structure was proposed in [22]. WPT across concrete and wooden walls was successfully implemented in BAPV systems. Nevertheless, the influence of walls containing metallic materials was not considered. Furthermore, the transmission distance remains limited and requires improvement to accommodate building PV systems with thicker walls.

The influence of the reinforced concrete structure of the building wall must be considered in the WPT system across the wall. The propagation of the electromagnetic field in the transmission direction is affected by the metal material in the wall, and the system loss is increased [23], [24]. Specifically, the equivalent resistance is significantly increased and the quality factor is substantially reduced. Therefore, effective strategies are required to mitigate these adverse effects. A multicoil inductive power repeater system was proposed in [25] to power sensor nodes embedded in reinforced concrete structures. Multiple load coils are used as power relays to enhance the magnetic field on the transmission path, and WPT with an efficiency of 47.7% is achieved. A new multicoil resonator design for a WPT system under reinforced concrete structure was proposed in [26]. Compared with the single-coil structure system, the transmission efficiency is further improved. A method to reduce the equivalent impedance of the rebar loop was proposed in [27]. The rebar array was used as a relay coil and the system transmission power was improved. However, the efficiency of WPT systems across reinforced concrete walls remains insufficient for the demanding requirements of BAPV applications and must be further improved.

The unique structure of autotransformers offers several advantages, including reduced spatial requirements, lower consumption of wiring materials, and decreased production costs, making them widely used in industrial applications. By changing the taps of the autotransformer to flexibly switch the windings, the output characteristics of the system are adjusted and the system state is reconstructed. In recent years, the application of autotransformers in the power electronics field has also attracted much attention. Autotransformers were used based on high-intensity-discharge lamp systems and magnetic ballasts in [28]. A design method for selecting autotransformer taps was proposed in [29] to suppress the startup transient current to a lower level. A hybrid converter that integrates soft-charging switched capacitors with an autotransformer was introduced in [30]. In addition, a multiport dc–dc autotransformer was developed in [31] for interconnecting multiple HVdc systems with varying voltage levels. Autotransformers have also been applied in multipulse ac–dc converters to enhance output performance [32], [33]. By extension, the application of autotransformer technology in the field of WPT can be a good way to improve parameter reconstruction capabilities.

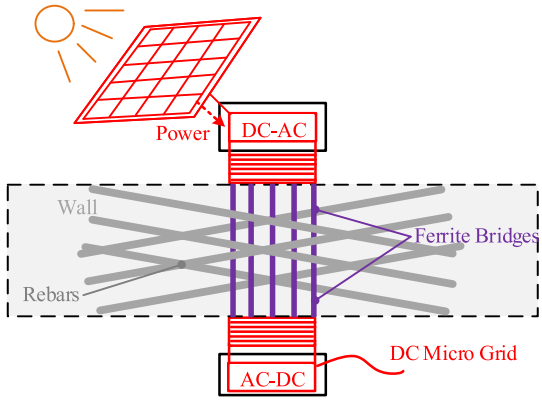

Fig. 1. Application scenarios of the novel BAPV-IPT system.

In summary, integrating IPT technology into BAPV systems offers a promising solution for connecting photovoltaic energy to the power grid. However, power losses caused by embedded metallic materials (such as rebars) within building walls must be addressed. Besides, the substantial thickness of building walls severely weakens the coupling coefficient between the coils. Furthermore, in view of the fact that the output voltage of photovoltaic panels fluctuates greatly due to the influence of light intensity [34], it is necessary to propose a solution that can realize system parameter reconstruction. To this end, a novel BAPV-IPT system based on WPT is proposed, as shown in Fig. 1. This system wirelessly connects outdoor PV components with the indoor dc microgrid. The system applies CSCs proposed in [16], which is represented by the red coil in Fig. 1. The purple part is a high-permeability ferromagnetic material that can be used as a building material to build into the concrete wall, eliminating the need for cable penetration. The major contributions of this work are summarized as follows.

1) Efficient WPT across reinforced concrete walls is achieved by the proposed BAPV-IPT system architecture. A strategy to reduce the adverse effects of rebars on the IPT system performance is proposed.
2) The coupling coefficient of the magnetic coupler across the building is significantly improved by the designed ferrite bridges (FBs). The transmission distance across the reinforced concrete wall is extended.
3) A reconfigurable parameter scheme for BAPV system is proposed. Dynamic system adaptability is achieved by switching winding taps in response to varying input conditions.

Contents of the other sections of this article are as follows. A magnetic coupling structure based on FB is proposed in

Section II. Considering the influence of the rebar array inside the wall, the feasibility of the system is demonstrated. In Section III, a parametrically reconfigurable magnetic coupling structure of multitap auto-coupling coils is proposed, a parametrically reconfigurable BAPV-IPT system is constructed, and the circuit model and loss characteristics are analyzed. In Section IV, a prototype of the system is constructed, and the feasibility of the proposed related technologies is verified through experimental analysis. Finally, Section V concludes this article.

II. Magnetic Coupling Structure Analysis and Design

A. Analysis and Design of the FB

The output power and PTE of the two-stage IPT system are determined by the system's coupling coefficient and quality factor [12]

$$P_L = \frac{L_2}{L_1}|U_1|^2 \frac{R_L}{(\omega L_2 + X_L)^2 + R_L^2} k^2 \tag{1}$$

$$\eta = \frac{k^2 Q_1 Q_2}{\left(1 + \sqrt{1 + k^2 Q_1 Q_2}\right)^2}. \tag{2}$$

Among them, R_L and X_L are the resistance and reactance of the load, respectively. U_1 is the input voltage. P_L and η are the output power and PTE of the system, respectively. L_1 and Q_1 are the self-inductance and quality factor of the transmitting coil, and L_2 and Q_2 are the self-inductance and quality factor of the receiving coil. k is the coupling coefficient between the coils.

In Formula (1), the output power of the IPT system is positively correlated with k. However, since the magnetic reluctance of the air outside the coil is large, the propagation of the magnetic field is significantly hindered. The magnetic flux can be effectively guided by ferrite cores with extremely high magnetic permeability. Therefore, introducing ferrite cores into the magnetic path to increase coupling coefficient is an effective way to achieve high-power energy transmission. Furthermore, the presence of rebars in the wall introduces reflected resistance into the circuit, increasing the coil's equivalent resistance. According to $Q = \omega L/R$, the quality factor of the coil is reduced by the rebars. From Formula (2), the PTE of the IPT system is positively correlated with Q and k. Therefore, the adverse effect of the reduction of Q on the PTE can be compensated by increasing k. It is worth noting that concrete has negligible influence on the IPT system according to [23]. In summary, FB is proposed to obtain a high level of k, guide the magnetic flux through the wall, and ensure that the BAPV system can achieve high-power and high-PTE through the wall.

In order to explore the relationship between k and ferrite cores, finite element method (FEM) is performed using ANSYS Maxwell. The transmission distance is set to 360 mm to simulate the wall thickness, and the ferrite core simulation parameters are consistent with TDK PC95. The specific simulation parameters are shown in Table I.

The relationship between k and the number of ferrite cores is shown in Fig. 2(a). The ferrite cores used are of standard commercial dimensions commonly found in products. The ferrite cores are coaxially placed at equal angles, and the distance between opposing ferrite cores is 190 mm. A significant increase in k is observed as the number of ferrite cores increases from 0 to 16. However, as the number of ferrite cores continues to increase, the incremental improvement in k diminishes. Therefore, 16 ferrite cores have the best effect on enhancing the coupling performance. However, k is at a low level of about 0.025. FB is designed to further enhance the coupling performance of the system. L_{FB} and L_{FO} are the lengths of the FB and the ferrite core outside the coil, respectively. The simulation results of the coupling coefficient for different lengths of ferrite cores are shown in Fig. 2(b). The coupling coefficient growth rate $\Delta\gamma$ is defined as

$$\Delta\gamma = \frac{dk}{dL_F} \tag{3}$$

where $L_F = L_{\mathrm{FB}} + L_{\mathrm{FO}}$. When $L_{\mathrm{FB}} = 360$ mm, $L_{\mathrm{FO}} = 0$ mm, the coupling coefficient exhibits a sharp increase, and the corresponding $\Delta\gamma$ reaches the maximum value. As the L_{FO} increases, k gradually rises. However, the $\Delta\gamma$ is much weaker than that of $L_{\mathrm{FO}} = 0$ mm. Ferrite cores outside the coils contribute only marginally to the improvement of coupling performance. Considering the comprehensive cost, the length of FB is designed at 360 mm, and the L_{FO} is 0 mm.

TABLE I
Parameters Utilized in the Simulations

Parameter	Value	Parameter	Value
Coil Diameter	220 mm	FB length	0 to 360 mm
Coil Height	180 mm	Coil Turns	28
Power Transfer Distance	360 mm	Ferrite Cross Section	5×15 mm^2

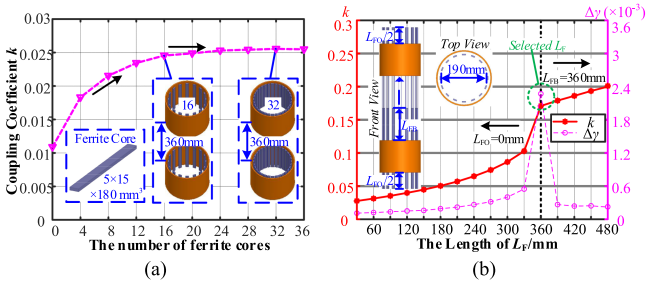

Fig. 2. Influence of different parameters of ferrite cores on coupling coefficient k. (a) Number of ferrite cores. (b) Length of ferrite cores.

B. Analysis of the Impact of Eddy Currents in Rebars

Due to the presence of metal materials such as rebars in the wall, the transmission characteristics of the IPT system are affected. To investigate the influence of rebars on the IPT system, FEM is performed in ANSYS Maxwell. Comparative simulations are established for both rebar loops and unconnected discrete rebars. The simulation parameters are consistent with those listed in Table I.

The magnetic field distribution cloud diagram of FEM is shown in Fig. 3. H is the relative height between the transmitting coil and the center of the rebar loop. The rebars are stacked vertically across each other. l is the side length of the closed

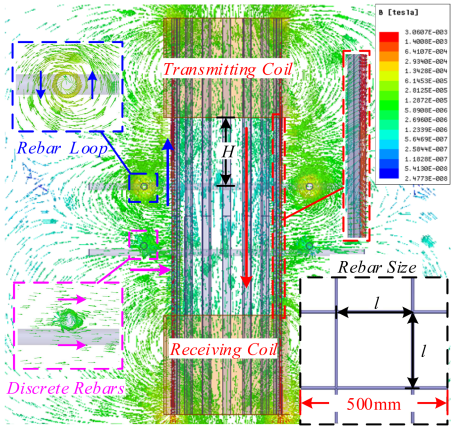

Fig. 3. Magnetic field vector distribution of a magnetic coupling structure with rebar loop and discrete rebars.

area enclosed by the rebars. The total length of a single rebar is 500 mm and the diameter is 12 mm. The rebar loops and discrete rebars are symmetrically distributed on the FB with an interval of 120 mm. A large amount of magnetic flux flows through FB, and the direction of the magnetic field is shown by the red arrow. Besides, the magnetic flux passes through the rebar loop to form eddy currents and excite a magnetic field in the opposite direction of propagation, as shown by the blue arrows. The reverse magnetic field has a negative impact on the coupling strength of the IPT system. However, the unconnected discrete rebars are not connected into a loop, and the loop eddy current is not formed. Due to the low magnetic reluctance of the rebar, part of the magnetic flux is gathered and guided to the vicinity of the FB, as shown by the magenta arrow in Fig. 3. The coupling coefficient of the IPT system is slightly enhanced.

The influence of the rebar loop and discrete rebars on the coupling coefficient is further analyzed using the FEM. Multiple groups of rebars are uniformly distributed vertically along the FB. The coupling coefficient change rate Δk is defined as

$$\Delta k = \frac{k_{\text{current}} - k_0}{k_0} \times 100\%. \tag{4}$$

Among them, k_0 is the coupling coefficient when there is no rebars, and k_{current} is the actual coupling coefficient during the rebars change process.

The existence of the rebar loop causes the coupling coefficient k to be severely reduced as shown in Fig. 4(a). An exaltation in $|\Delta k|$ is observed as the side length of rebar loop reduces. Since the generated eddy current increases with the decrease in the distance from the magnetic coupling structure, the weakening effect on the original magnetic field enhances. Similarly, the exaltation in the number of rebar loops leads to an aggravated drop in k. The influence of discrete rebars on k is tiny as shown in Fig. 4(b). And there are some positive values of Δk, indicating that the coupling coefficient is slightly improved. Moreover, the greater the number of discrete rebars and the closer they are to the magnetic coupling structure, the greater the increase in magnetic coupling strength.

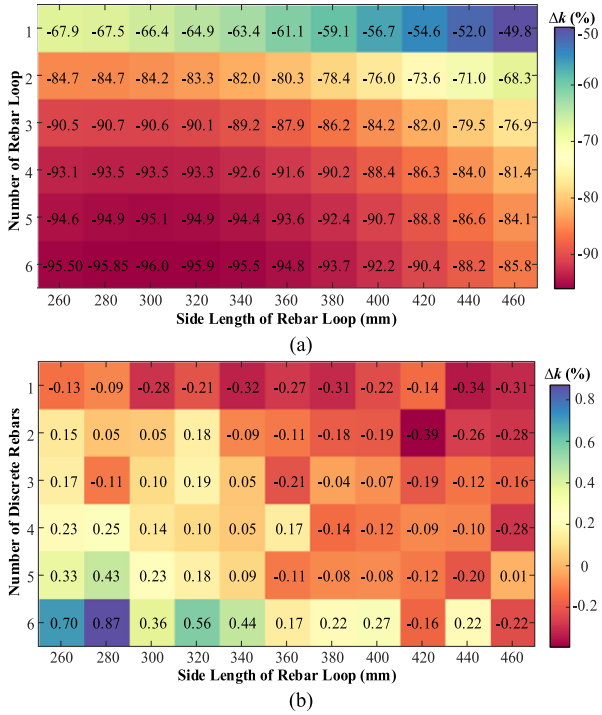

Fig. 4. Influence of different numbers of rebar loops and discrete rebars on the coupling coefficient. (a) Rebar loop. (b) Discrete rebars.

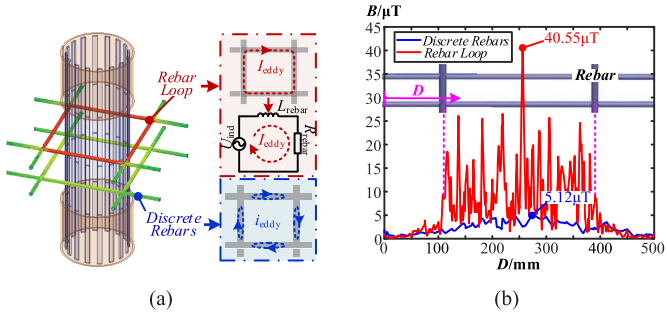

Fig. 5. Eddy current loss simulation results of rebar loop and discrete rebars. (a) Eddy current loss distribution. (b) Magnetic flux density on rebar.

As soft magnetic materials, rebars exhibit both eddy current losses and hysteresis losses. In systems operating above 60 kHz, eddy current losses dominate the total magnetic losses in rebars. The eddy current loss P_{eddy} can be expressed as [23]

$$P_{\text{eddy}} = K_e (f B_m)^2 V_{\text{rebar}}. \tag{5}$$

Among them, K_e is an empirical parameter related to the material. f is the operating frequency of the system. B_m is the peak value of the magnetic flux density. V_{rebar} is the effective volume of the rebars under the action of the magnetic field.

In order to further analyze the eddy current loss on the rebars, the model same as Fig. 3 is simulated using ANSYS Maxwell software shown in Fig. 5.

The eddy current losses generated on the rebar loop and discrete rebars are significantly different at the same scale as shown in Fig. 5(a). According to Formula (5), P_{eddy} is determined by

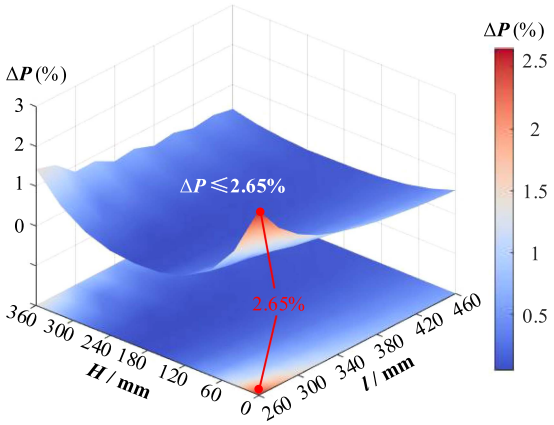

Fig. 6. Simulation results of ΔP.

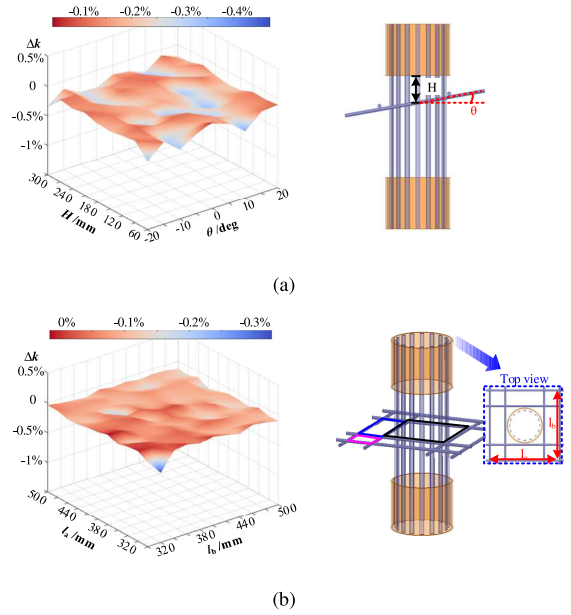

Fig. 7. Effect of discrete rebars misalignment on coupling. (a) Angular misalignment. (b) Horizontal misalignment.

the peak magnetic flux density B_m under the condition that the V_{rebar}, K_e, and f are the same. Different from discrete rebars, the noninsulated closed circuit is formed by the rebar loop and exhibits similar characteristics to a single-turn coil. Therefore, the rebar loop can be equivalent to a series circuit of an inductor L_{rebar} and a resistor R_{rebar}. At this time, magnetic field coupling is formed between the rebar loop and the coils. However, the magnetic field coupling between the discrete rebars and the coils is extremely weak. The magnetic flux density on the rebar loop is much greater than that on the discrete rebars as shown in Fig. 5(b). Since P_{eddy} and $B2$ m are directly proportional, this difference is further amplified. As a result, the eddy current loss on the discrete rebars is much weaker than that on the rebar loop.

In order to further verify the above analysis, the eddy current loss change rate ΔP is defined to show the difference in eddy current loss more intuitively

$$\Delta P = \frac{P_{\text{S\_rebar}}}{P_{\text{L\_rebar}}} \times 100\% \tag{6}$$

where $P_{\text{S\_rebar}}$ and $P_{\text{L\_rebar}}$ are the eddy current losses of discrete rebars and rebar loop during the change process.

The simulation results of eddy current loss change rate ΔP are shown in Fig. 6. It is evident that the maximum ΔP reaches only 2.65%, indicating that under the same conditions, $P_{\text{S\_rebar}} \ll P_{\text{L\_rebar}}$.

In summary, the problem of reduced coupling coefficient caused by Lenz law can be solved by insulating the rebar loops, and the eddy current loss can be reduced by 2–3 orders of magnitude. Therefore, the rebar connection nodes near the magnetic coupling structure need to be filled and isolated with insulating materials in the BAPV-IPT system. The structural performance of reinforced concrete walls is not affected by tiny material infills.

In practical installation scenarios, angular and horizontal misalignments may occur between the rebars and the magnetic coupling structure. It is necessary to study the influence of rebars misalignment on the magnetic coupling performance. The corresponding simulation results are shown in Fig. 7. Δk is expressed as Formula (4). The inclination angle θ of the rebar varies within the range of $\pm 20°$. The side lengths of rebar array l_a and l_b vary within the range of 300–500 mm. When the discrete rebars are angular misaligned at different heights H by $[-20^{\circ}, 20^{\circ}]$, $-0.47\% \leq \Delta k \leq -0.04\%$ as shown in Fig. 7(a). Multiple noncoaxial regions are generated under the horizontal misalignment of the rebars, $-0.33\% \leq \Delta k \leq 0.01\%$ as shown in Fig. 7(b). The impact on the coupling performance when the discrete rebars are misaligned is negligible. Therefore, the proposed magnetic coupling structure shows high tolerance to spatial misalignment of the rebars after the rebar connection nodes are insulated.

III. Analysis of IPT System Based on Multitap Parameter Reconfiguration

A. Analysis of BAPV-IPT System Based on Multitap Parameter Reconfiguration

Based on the design of FB and the influence of rebars on the IPT system in Section II, a multitap parameter reconfigurable IPT system architecture is proposed in Fig. 8 to transfer power across the wall. The specific application scenario is shown in Fig. 8(a). Photovoltaic panels can be flexibly arranged in multiple arrays as needed. Power transfer across the wall from multiple sets of photovoltaic panels can be achieved with a single set of coils. More details are shown in Fig. 8(b), embedding the FB in the wall provides a clear low reluctance path for the magnetic flux. Since no current flows through the ferrite core, leakage currents and the formation of thermal bridges are avoided. Moreover, Mn-Zn ferrite is a durable solid material suitable for integration into concrete structures as a building material. Therefore, problems such as water seepage caused by cable penetration are avoided, and maintenance and repair costs are reduced. In addition, the output voltage of photovoltaic power generation components is inevitably affected by light

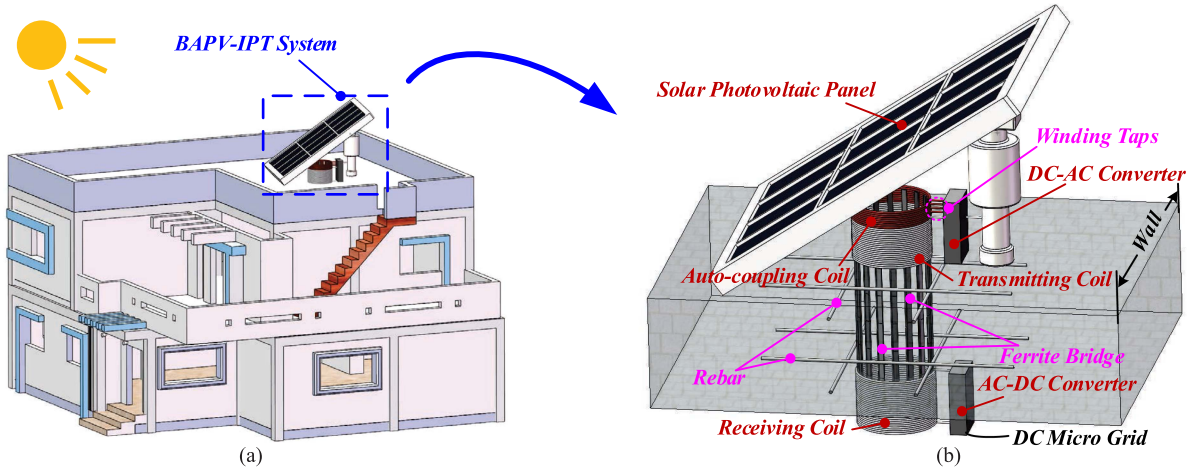

Fig. 8. BAPV-IPT system structure based on multitap parameter reconfigurable coil. (a) Application scenarios. (b) Details of the BAPV-IPT system.

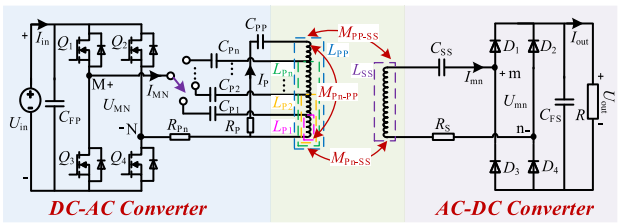

Fig. 9. Circuit model of BAPV-IPT system based on multitap parameter reconfigurable coil.

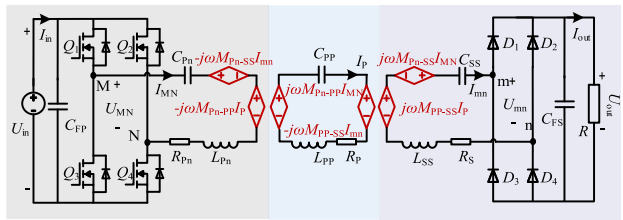

Fig. 10. Circuit model of BAPV-IPT system with controlled sources.

and temperature, which poses challenges to the stability of the building's microgrid. The principle of autotransformer is introduced into BAPV-IPT system, and the output characteristics of the system are adjusted by changing the winding tap. Flexible parameter adjustment can resist the influence of environmental factors on photovoltaic power generation components. In addition, the auto-coupling coil shares a common tap with the transmitting coil, and the adjacent rebar loops near the FB have been insulated.

With the proposed magnetic coupling structure and system design, the BAPV-IPT system can effectively overcome these challenges, leading to an expected improvement in PTE across reinforced concrete walls. Moreover, the self-inductance of the coils is increased by the ferrite cores, and the reactive power loss generated thereon cannot be ignored. In order to further improve the PTE of the IPT system, it is necessary to perform reactive power compensation from the circuit topology.

The system equivalent circuit is shown in Fig. 9. The microgrid in the building connected to the dc output side is represented by the load R in the analysis. U_{in} is the output voltage of the solar photovoltaic power generation component. The corresponding self-inductances of the auto-coupling coil, transmitting coil, and receiving coil are represented by L_{Pn}, L_{PP}, and L_{SS}, respectively. The compensation capacitors for the coils are C_{Pn}, C_{PP}, and C_{SS}. $M_{\text{Pn-PP}}$, $M_{\text{PP-SS}}$, and $M_{\text{Pn-SS}}$ are the mutual inductances between the corresponding coils. Q_1–Q_4 are power MOSFET switches, D_1–D_4 are switch diodes, C_{FP} and C_{FS} are filter capacitors. R_{Pn}, R_P, and R_S are the equivalent series resistance (ESR) of each coil and their compensation capacitor.

According to the operating characteristics of the full-bridge inverter circuit and the rectifier circuit, the dc side parameters can be equivalent to the ac side as [35]

$$U_{\text{MN}} = \frac{2\sqrt{2}U_{\text{in}}}{\pi},\ U_{\text{mn}} = \frac{2\sqrt{2}U_{\text{out}}}{\pi},\ R_{\text{eq}} = \frac{8R}{\pi^2}. \tag{7}$$

The system circuit is equivalent to a controlled source model as shown in Fig. 10 to analyze the output characteristics of the multitap parameter reconfigurable IPT system. The corresponding circuit state equation is expressed as, (8) shown at the bottom of the next page.

According to the series resonance condition [36], the compensation capacitor is as

$$\frac{1}{\omega C_{\text{xn}}} = \omega L_{\text{xn}} \quad x = P, S.\ \ n = P, S, 1, 2, 3 \ldots. \tag{9}$$

The circuit state equation is simplified to the following equation:

$$\begin{pmatrix} U_{\text{MN}} \\ 0 \\ 0 \end{pmatrix} = \begin{pmatrix} R_{\text{Pn}} & -j\omega M_{\text{Pn-PP}} & -j\omega M_{\text{Pn-SS}} \\ -j\omega M_{\text{Pn-PP}} & R_P & -j\omega M_{\text{PP-SS}} \\ -j\omega M_{\text{Pn-SS}} & -j\omega M_{\text{PP-SS}} & R_S + R_{\text{eq}} \end{pmatrix} \times \begin{pmatrix} I_{\text{MN}} \\ I_P \\ I_{\text{mn}} \end{pmatrix}. \tag{10}$$

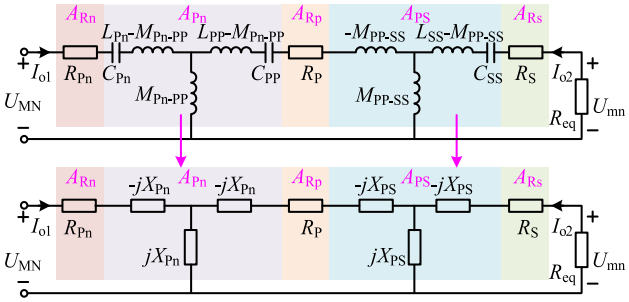

Fig. 11. Equivalent T^2 circuit model.

Therefore, the output characteristic of the multitap parameter reconfigurable IPT system is expressed as

$$\left|\frac{U_{mn}}{U_{MN}}\right| = \left|\frac{j\omega R_{eq}(M_{Pn-SS}R_P + j\omega M_{Pn-PP}M_{PP-SS})}{\omega^2 M_{Pn-PP}[M_{Pn-PP}(R_S+R_{eq}) + 2j\omega M_{PP-SS}M_{Pn-SS}] + \omega^2(M_{PP-SS}^2 R_{Pn} + M_{Pn-SS}^2 R_P) + R_{Pn}R_P(R_S+R_{eq})}\right|. \tag{11}$$

Compared to other circuit parameters, ESR at each stage of the circuit is relatively small. Therefore, R_{Pn}, R_P, R_S in Formula (11) are ignored to simplify the analysis of the output characteristics

$$\left|\frac{U_{mn}}{U_{MN}}\right| = \left|-\frac{M_{PP-SS}R_{eq}}{M_{Pn-PP}R_{eq} + 2j\omega M_{PP-SS}M_{Pn-SS}}\right|. \tag{12}$$

Due to the characteristics of the autotransformer and loosely coupled magnetic structure, the smaller number of auto-coupling coil turns can make $M_{Pn\text{-}PP}$ much higher than $M_{PP\text{-}SS}$ and $M_{Pn\text{-}SS}$. When $M_{Pn\text{-}PP}R_{eq}$ is much larger than $2\omega M_{PP\text{-}SS}M_{Pn\text{-}SS}$, the imaginary part in the denominator of Formula (12) has little effect on the voltage transformation ratio G, and the cross-coupling $M_{Pn\text{-}SS}$ can be ignored. Under this condition, the multitap parameter-reconfigurable IPT system exhibits a constant voltage output characteristic.

B. Analysis of the Equivalent T^2 Circuit

After neglecting $M_{Pn\text{-}SS}$, according to the decoupling equivalent principle, the multistage circuit is simplified to the equivalent T^2 circuit shown in Fig. 11. The equivalent T^2 circuit is a two-port network that exhibits linear passive characteristics. The resonant parameters of the T^2 circuit are as

$$X_{Pn} = \omega M_{Pn-PP} = \omega M_{Pn-PP} + \frac{1}{\omega C_{Pn}} - \omega L_{Pn}$$
$$= \omega M_{Pn-PP} + \frac{1}{\omega C_{PP}} - \omega L_{PP} \tag{13a}$$

$$X_{PS} = \omega M_{PP-SS} = \omega M_{PP-SS} + \frac{1}{\omega C_{SS}} - \omega L_{SS}. \tag{13b}$$

The injected currents on both sides of the two-port network are I_{o1} and I_{o2}, then the network can be described as

$$\begin{bmatrix} U_{MN} & I_{o1} \end{bmatrix}^T = A_G \begin{bmatrix} U_{mn} & -I_{o2} \end{bmatrix}^T \tag{14}$$

where A_G is the overall transmission parameter matrix, and $I_{o1} = I_{MN}, I_{o2} = -I_{mn}$. A_{Rn}, A_{Rp}, and A_{Rs} are composed of the ESR of the auto-coupling coil, the transmitting coil, and the receiving coil, respectively. A_{Pn} is composed of the self-inductance and compensation capacitance of the auto-coupling coil and the transmitting coil, and the mutual inductance between them. A_{PS} is composed of the self-inductance and compensation capacitance of the receiving coil, and the mutual inductance between the transmitting coil and the receiving coil.

According to the two-port network theory, the transmission parameter matrices are obtained as

$$A_{Rn} = \begin{pmatrix} 1 & R_{Pn} \\ 0 & 1 \end{pmatrix} A_{Rp} = \begin{pmatrix} 1 & R_P \\ 0 & 1 \end{pmatrix} A_{Rs} = \begin{pmatrix} 1 & R_S \\ 0 & 1 \end{pmatrix}$$
$$A_{Pn} = \begin{pmatrix} 0 & -jX_{Pn} \\ 1/X_{Pn} & 0 \end{pmatrix} A_{PS} = \begin{pmatrix} 0 & -jX_{PS} \\ 1/X_{PS} & 0 \end{pmatrix}. \tag{15}$$

The transmission parameter matrix A_G is obtained as

$$A_G = A_{Rn}A_{Pn}A_{Rp}A_{PS}A_{Rs} = \begin{pmatrix} a & b \\ c & d \end{pmatrix} \tag{16a}$$

$$\begin{cases} a = -(\omega^2 M_{Pn-PP}^2 + R_{Pn}R_P)/(\omega^2 M_{Pn-PP}M_{PP-SS}) \\ b = -[R_{Pn}R_PR_S + \omega^2(R_S M_{Pn-PP}^2 + R_{Pn}M_{PP-SS}^2)]/(\omega^2 M_{Pn-PP}M_{PP-SS}) \\ c = -R_P/(\omega^2 M_{Pn-PP}M_{PP-SS}) \\ d = -(\omega^2 M_{PP-SS}^2 + R_PR_S)/(\omega^2 M_{Pn-PP}M_{PP-SS}) \end{cases}. \tag{16b}$$

Therefore, the efficiency of the T^2 circuit is solved as (17) shown at the bottom of the next page.

When R_{Pn}, R_P, and R_S are equal to zero, the voltage conversion ratio G of the BAPV-IPT system is expressed as

$$G = \left|\frac{U_{out}}{U_{in}}\right| = \left|\frac{U_{mn}}{U_{MN}}\right| = \frac{M_{PP-SS}}{M_{Pn-PP}}. \tag{18}$$

Formula (18) shows that the G is only affected by $M_{PP\text{-}SS}$ and $M_{Pn\text{-}PP}$. The output characteristics can be changed by adjusting $M_{Pn\text{-}PP}$. In order to more clearly show the output characteristics of the BAPV-IPT system, each mutual inductance is obtained by ANSYS Maxwell. The simulation modeling parameters are shown in Table II, and the other parameters are the same as before.

$$\begin{pmatrix} U_{MN} \\ 0 \\ 0 \end{pmatrix} = \begin{pmatrix} j\omega L_{Pn} + \frac{1}{j\omega C_{Pn}} + R_{Pn} & -j\omega M_{Pn-PP} & -j\omega M_{Pn-SS} \\ -j\omega M_{Pn-PP} & j\omega L_{PP} + \frac{1}{j\omega C_{PP}} + R_P & -j\omega M_{PP-SS} \\ -j\omega M_{Pn-SS} & -j\omega M_{PP-SS} & j\omega L_{SS} + \frac{1}{j\omega C_{SS}} + R_S + R_{eq} \end{pmatrix} \begin{pmatrix} I_{MN} \\ I_P \\ I_{mn} \end{pmatrix}. \tag{8}$$

TABLE II
PARAMETERS UTILIZED IN THE SIMULATIONS

Parameter	Value	Parameter	Value
Transmitting Coil Height	240 mm	Auto coupling Coil Turns	2—46
Transmitting Coil Turns	46	Wire Diameter	5.22 mm

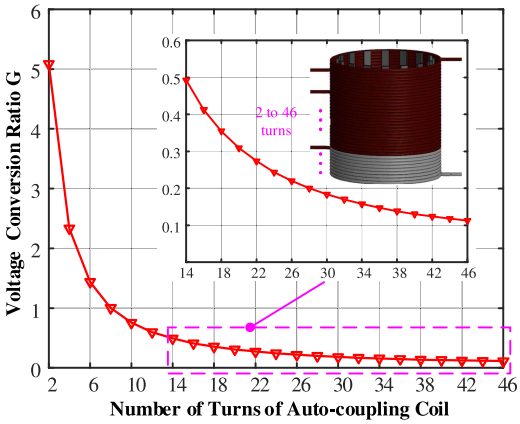

Fig. 12. Voltage conversion ratio G of the BAPV-IPT system changes with different turns of auto-coupling coil.

Based on the mutual inductances $M_{\text{PP-SS}}$ and $M_{\text{Pn-PP}}$ obtained by FEM, the voltage conversion ratio G corresponding to the autocoupling coil with different numbers of turns is shown in Fig. 12. The various voltage conversion ratios G prove that the proposed BAPV-IPT system based on multitap parameter reconfiguration has a high degree of design freedom and system reconstruction flexibility.

C. IPT System Loss Analysis

The efficiency of the T^2 circuit has been obtained by Formula (17) shown at the bottom of this page, but only the copper loss P_{Cu} is taken into account. The inverter circuit loss P_{INV}, the rectifier circuit loss P_{REC}, and the core loss P_{core} are not included.

Depending on the model of the MOSFET switches and diodes, P_{INV} and P_{REC} can be calculated as [16]

$$P_{\text{INV}} = 2R_{M(\text{on})}I_{\text{in}}^2 \tag{19}$$

$$P_{\text{REC}} = 2\left(\frac{2\sqrt{2}}{\pi}U_{D(\text{on})}I_{\text{out}} + R_{D(\text{on})}I_{\text{out}}^2\right). \tag{20}$$

Among them, $R_{M(\text{on})}$ and $R_{D(\text{on})}$ are the on-resistance of the MOSFET and diode respectively, and $U_{D(\text{on})}$ is the forward voltage drop across the switch diode.

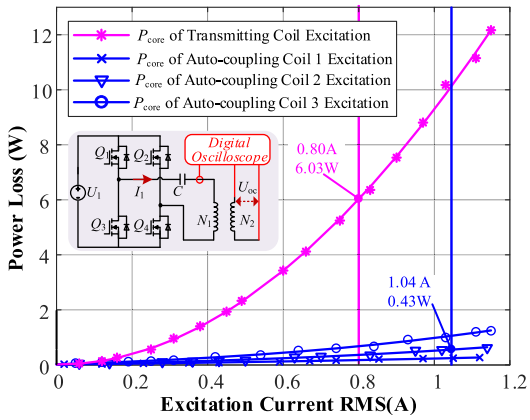

Fig. 13. Core loss curve of BAPV-IPT system measured by large signal characterization method.

Since a large number of ferrite cores are used in magnetic coupling structures, the resulting core loss P_{core} must be taken into consideration. The core loss is composed of hysteresis loss, eddy current loss and excess loss, showing strong nonlinear characteristics. Therefore, quantifying P_{core} is highly complex and challenging. A large-signal characterization method for measuring core losses was proposed in [37] and [38]. Through the primary side series resonance and the secondary side open circuit, the primary side input current $I_1(t)$ and the secondary side open circuit voltage $U_{\text{oc}}(t)$ are obtained. The core loss can be obtained by integrating as follows [37]:

$$P_{\text{core}} = f\frac{N_1}{N_2}\int_0^T I_1(t)U_{\text{oc}}(t)dt \tag{21}$$

where f and T are the operating frequency and cycle time of the inverter. f is 100 kHz to be consistent with the actual operating frequency of the proposed BAPV-IPT system. N_1, N_2 are the turns of the excitation side coil and the open circuit side coil.

Taking the three-tap autocoupling IPT system as an example, the large signal characterization measurement method is used to obtain P_{core}. Due to the reconfigurable characteristics of the proposed BAPV-IPT system, the core loss caused by each autocoupling coil is different. In addition, the receiving coil is coupled with both the transmitting coil and the autocoupling coils. The core loss of the transmitting coil and each autocoupling coil needs to be measured. The experimental results and fitting curves are shown in Fig. 13. The winding taps 1, 2, 3 are designed at the 6th, 10th, and 14th turns, respectively. The current on each coil measured under normal working conditions is matched with the current in Fig. 13 to obtain the corresponding core loss P_{core}.

$$\begin{aligned}\eta_{T^2} &= \frac{I_{\text{mn}}^2 R_{\text{eq}}}{U_{\text{MN}}I_{\text{MN}}} = \frac{R_{\text{eq}}}{(aR_{\text{eq}}+b)(cR_{\text{eq}}+d)} \\ &= \frac{\left(M^2{}_{\text{Pn-PP}}M^2{}_{\text{PP-SS}}R_{\text{eq}}\omega^4\right)/\left(M^2{}_{\text{PP-SS}}\omega^2 + R_{\text{eq}}R_P + R_PR_S\right)}{\omega^2\left(M^2{}_{\text{Pn-PP}}R_{\text{eq}} + M^2{}_{\text{PP-SS}}R_{\text{Pn}} + M^2{}_{\text{Pn-PP}}R_S\right) + R_{\text{eq}}R_PR_{\text{Pn}} + R_PR_{\text{Pn}}R_S}.\end{aligned} \tag{17}$$

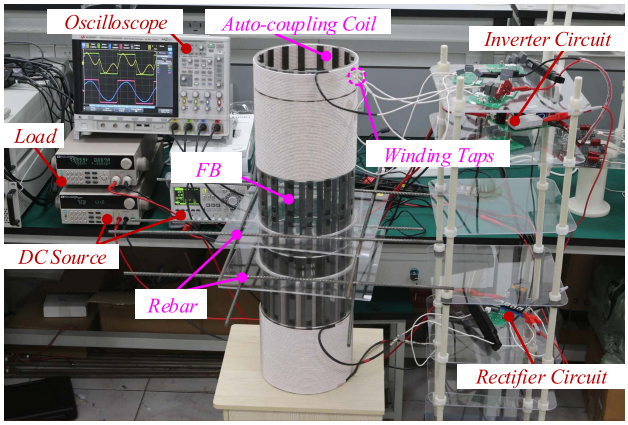

Fig. 14. Prototype of the BAPV-IPT system based on three-tap parameter reconfigurable coils.

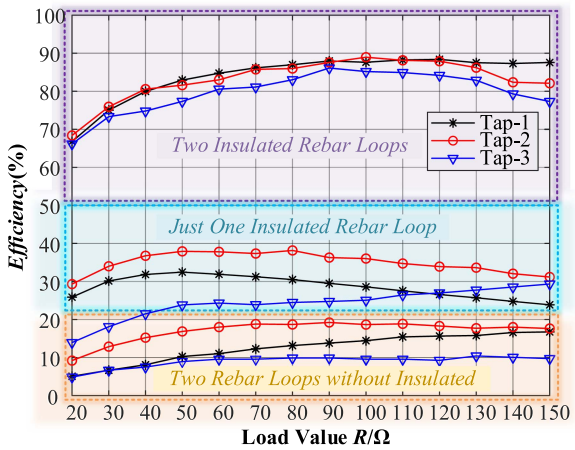

Fig. 15. Comparative experiment on the influence of rebar loop eddy loss on BAPV-IPT system.

TABLE III
PARAMETERS OF THE SYSTEM

Parameter	Value	Parameter	Value
f	100 kHz	C_{P3}	17.8 nF
Q_1-Q_4	IRFBA22N50	L_{PP}	1394.2 μH
D_1-D_4	MBR40200WT	R_{PP}	1.64 Ω
Ferrite Core	PC 95	C_{PP}	1.81 nF
L_{P1}	27.46 μH	L_{SS}	571.8 μH
R_{P1}	404 mΩ	R_{SS}	1.06 Ω
C_{P1}	91.1 nF	C_{SS}	4.26 nF
L_{P2}	73.44 μH	$M_{P1\text{-}PP}$	103.2 μH
R_{P2}	140 mΩ	$M_{P2\text{-}PP}$	196.3 μH
C_{P2}	34.5 nF	$M_{P3\text{-}PP}$	301.5 μH
L_{P3}	141.56 μH	$M_{PP\text{-}SS}$	148.5 μH
R_{P3}	245 mΩ		

IV. EXPERIMENTAL VERIFICATION OF IPT SYSTEM

Based on the multitap parameter reconfigurable BAPV-IPT system and T^2 compensation topology circuit described above, an experimental prototype is constructed as shown in Fig. 14. Similarly, three winding taps are set on the transmitting coil side, and the number of turns is set the same as when measuring magnetic loss using the large signal characterization method.

The transmitting coil height is 240 mm and the number of turns is 46. The receiving coil height is 180 mm and the number of turns is 28. All coils share a uniform diameter of 220 mm. The transmission distance and the length of FB are set to 360 mm to simulate passing through a 360-mm building wall. In addition, identical discrete rebars are symmetrically arranged on the FB to replicate the embedded reinforcement structure, with their connection nodes insulated using appropriate materials. The specific parameters of the system prototype are shown in Table III.

The effect of eddy current losses in the rebar loops during power transfer on the BAPV-IPT system is experimentally studied. The PTE of the system under different conditions is shown in Fig. 15. A standard safety voltage of 36 V is applied. The connection points of the rebar loop are filled with insulating materials, which is insulated rebar loop. As depicted in Fig. 15, significant eddy current losses are induced in the uninsulated rebar loop, leading to a substantial reduction in the system's PTE. When both sets of rebar loops are not insulated, the PTE drops below 20%. When only one set of rebar loop is insulated, the PTE is less than 40%. Such low efficiency falls short of the operational requirements of the BAPV-IPT system. The rebar loops are insulated without affecting the structural performance of the reinforced concrete wall. With full insulation, the system's PTE reaches approximately 90%.

The ability of the proposed BAPV-IPT system to resist PV output voltage fluctuations caused by factors such as illumination is experimentally verified. The input voltage U_{in} is set to 72, 120, and 192 V to simulate the varying output voltage of the PV panel. The dynamic response process waveforms of the system output voltage are shown in Fig. 16. The relay connected to the winding taps is controlled by the TMS320F28035 to achieve system parameter reconstruction. The switching of the winding taps is performed automatically when a deviation in the output voltage is detected. As shown in Fig. 16, the input voltage fluctuates in a wide range of 72—192 V, and the output voltage of the system is stabilized within an extremely low fluctuation range. Resistance to fluctuations in the output voltage of the PV panel is achieved.

In addition, the transmission characteristics of the three-tap parameter reconfigurable BAPV-IPT system are experimentally verified, and the experimental results corresponding to different winding taps are shown in Fig. 17. As shown in Fig. 17(a), when 72 V dc voltage is injected into Tap-1 and $R = 20\ \Omega$, the system has a maximum output power of 225.16 W. When $R = 80\ \Omega$, $U_{\text{out}} = 83.16$ V, $P_{\text{out}} = 86.4$ W, the current flowing through the autocoupling coil, transmitting coil, and receiving coil is measured to be 1.04, 0.80, and 0.93 A. According to calculations, the total system loss is 9.6 W and P_{Cu} is 2.344 W. According to the core loss curve measured in Fig. 13, $P_{\text{core}} = 6.46$ W. At this time, the sum of P_{Cu} and P_{core} is 8.98 W, while P_{INV} and P_{REC} are usually between tens and hundreds of mW.

The output voltage curve in Fig. 17 shows that the system exhibits a constant voltage output characteristic, though a voltage climbing phenomenon occurs under light load conditions.

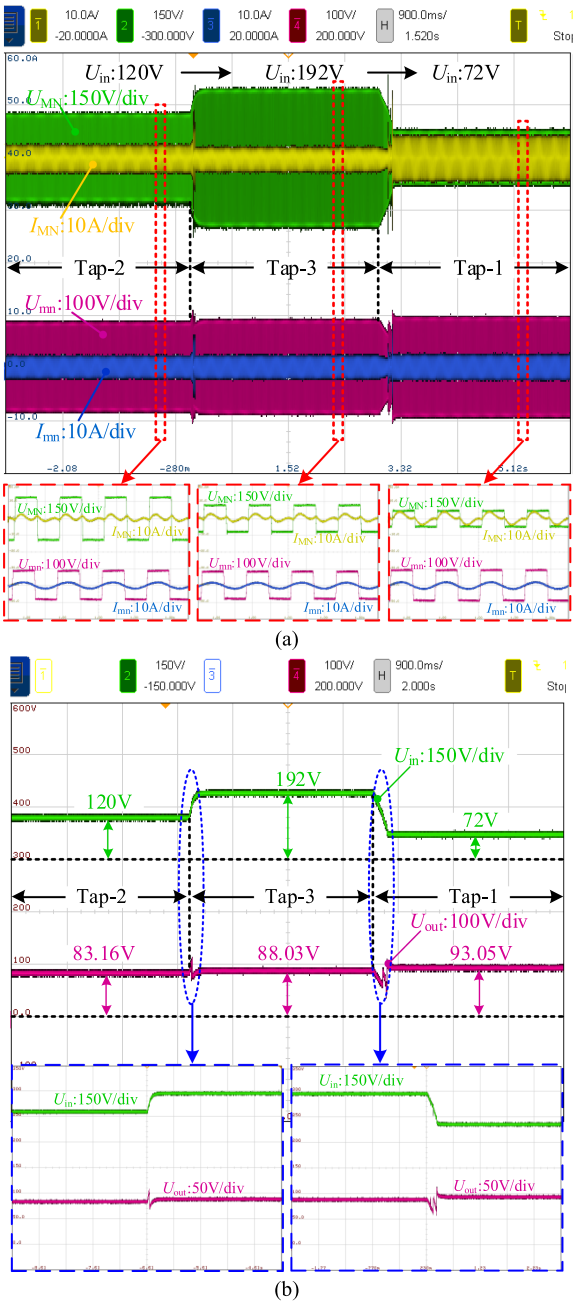

Fig. 16. BAPV-IPT system dynamic response process waveforms. (a) AC waveform. (b) DC waveform.

On the one hand, a large current flows through the coil, and the parasitic resistance produces a large voltage drop, causing U_{out} to decrease. In addition, the existence of $M_{\text{Pn-SS}}$ affects the output voltage, causing it to deviate from the ideal constant-voltage curve. As R increases, the current in each coil decreases, the voltage drops across the parasitic resistance decreases, and the influence of $M_{\text{Pn-SS}}$ on U_{out} becomes negligible. The magenta curve highlights the high efficiency of the proposed BAPV-IPT system. As R increases, the system's PTE initially increases and then slightly decreases. As shown in Fig. 17(b), when a 120-V dc voltage is injected into Tap-2 and $R = 80\ \Omega$, the system has a maximum efficiency of 90.01%.

The U_{out} of the system at different winding taps are stable under light loads when ESR and $M_{\text{Pn-SS}}$ is not considered as shown in Fig. 18. However, theoretical models that account for ESR or $M_{\text{Pn-SS}}$ exhibit a slight voltage climbing phenomenon under light load conditions. The system equivalent impedance is no longer completely resistive due to $M_{\text{Pn-SS}}$, and a portion of the voltage is dropped across the ESR. Consequently, U_{out} is reduced and deviates from the ideal constant voltage characteristic curve. The resistance value of the system equivalent impedance increases as R increases, and the influence of $M_{\text{Pn-SS}}$ is weakened. Moreover, the reduced current leads to a lower voltage drop across the ESR. At this time, U_{out} rises slightly and gradually approaches the ideal voltage value without ESR and $M_{\text{Pn-SS}}$. The experimental results are in close agreement with the output voltage curve when ESR and $M_{\text{Pn-SS}}$ are considered. The rationality of the above-mentioned analysis is verified.

The operating temperature of the proposed BAPV-IPT system is experimentally studied at an ambient temperature of approximately 23 °C. Eddy currents induced in the rebars are a key factor influencing the system's thermal behavior. The temperature distribution of the system with different rebar configurations is shown in Fig. 19. The system is operated continuously until thermal equilibrium is achieved. The temperature on the rebar loop increased by approximately 40 °C during this period as shown in Fig. 19(a)–(c). Such temperature rise may shorten the service life of the building walls and degrade the thermal insulation performance. In contrast, the temperature change of the discrete rebars in the process of reaching thermal equilibrium is not obvious, as shown in Fig. 19(d)–(f). This effectively eliminates potential thermal threats to the building structure. Furthermore, although a large amount of magnetic flux is confined to FB, the temperature on the ferrite cores remains consistent with the ambient temperature. The performance indicators of the ferrite cores can always remain unchanged during the operation of the BAPV-IPT system. Consequently, the operational stability of the system is ensured.

The representative waveforms of the BAPV-IPT system are presented in Fig. 20. The ac-side waveforms are shown in Fig. 20(a), (c), and (e). The ac side input voltage U_{MN} slightly leads the input current I_{MN}, indicating that soft switching is achieved by the MOSFETs. The output current I_{mn} has favorable sinusoidally and almost no harmonics, indicating excellent harmonic suppression performance of the proposed topology. In Fig. 20(b), (d), and (f), the dc side input voltage U_{in} and output voltage U_{out} remain relatively flat, while the dc side input current I_{in} and output current I_{out} are affected by the harmonics in the system and have certain fluctuations. Due to the filtering effect of filter capacitors C_{FP} and C_{FS}, the fluctuation of dc waveform is effectively constrained within a limited range.

In practical applications, the configuration of rebars is typically random. The tilted and nonuniformly spaced rebars configurations are experimentally investigated as shown in Fig. 21. Among them, State 1 is the same configuration as Fig. 14. State 2 and State 3 configure tilted and nonuniformly spaced discrete rebars, respectively. Based on the analysis in Section II, the influence of discrete rebars on the IPT system is minimal. Therefore, the differences between States 1, 2, and 3 in U_{out} and

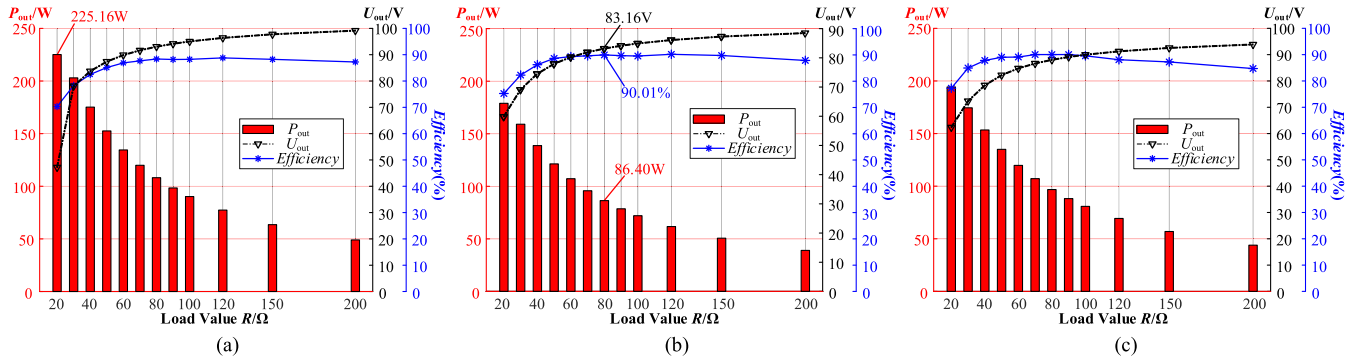

Fig. 17. Experimental results of the IPT system under different winding taps. (a) Tap-1, $U_{\rm in} = 72$ V. (b) Tap-2, $U_{\rm in} = 120$ V. (c) Tap-3, $U_{\rm in} = 192$ V.

TABLE IV
COMPARISON WITH SIMILAR WORKS IN RECENT YEARS

References	Distance	Efficiency (max)	Power (max)	Additional coil	Reconfigurability	Details
This Work	360 mm	90.01%	225.16 W	0	Yes	WPT across the Wall, Reinforced Concrete Wall, BAPV System
[22]	60 mm	83.4%	160 W	1	No	WPT across the wall, Wood and Concrete wall, BAPV system
[25]	515 mm	47.4%	About 2.4 W	2	No	Reinforced Concrete Wall, Power Relay, Structural Health Monitoring (SHM) System
[26]	300 mm	39%	10 W	8	No	Reinforced Concrete Wall, Multi-Coil Resonator, SHM system
[27]	200 mm	34.79%	2.67 W	1	Yes	Reinforced Concrete Wall, Changing Rebar Loop Equivalent Impedance, SHM System

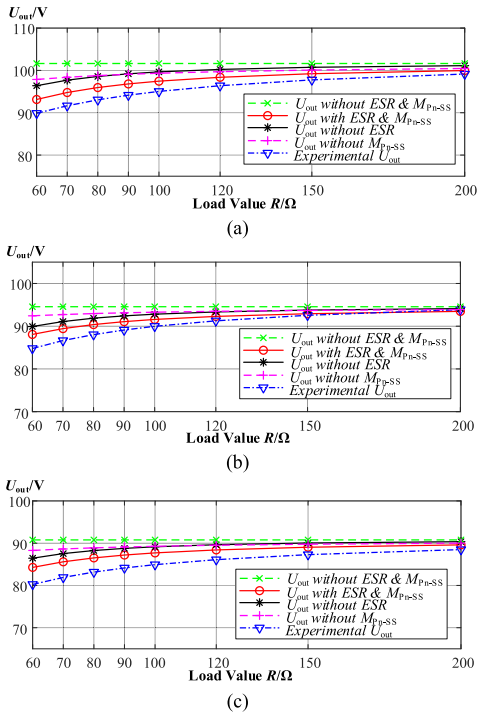

Fig. 18. Comparison of theoretical and experimental output voltage values. (a) Tap-1. (b) Tap-2. (c) Tap-3.

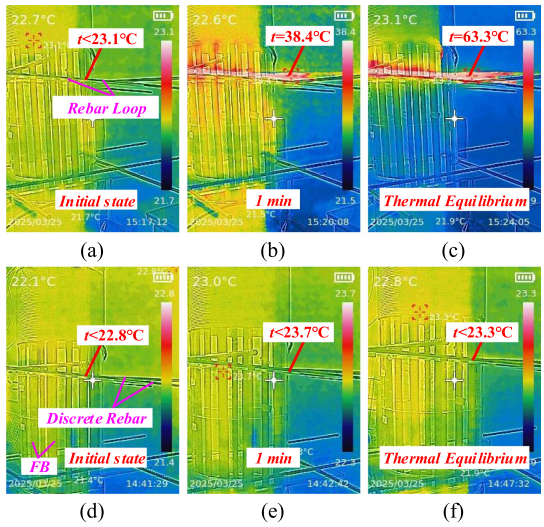

Fig. 19. Temperature distribution of the IPT system at different working times when Tap-1 is turned ON and $U_{\rm in} = 72$ V, $R = 50\ \Omega$. With rebar loops. (a) Initial state. (b) Work 1 min. (c) Thermal equilibrium. With discrete rebars. (d) Initial state. (e) Work 1min. (f) Thermal equilibrium.

PTE are extremely weak as shown in Fig. 21. The BAPV-IPT system exhibits a high tolerance to the spatial configuration of the rebars.

Also, the coil may have a slight spatial misalignment, causing the ferrite cores to become partially misaligned with the FB. The output characteristics of the IPT system under horizontal and angular coil misalignment conditions are shown in Fig. 22. When the misalignment distance $\alpha = 3$ mm and the misalignment angle $\beta = 5°$, $U_{\rm out}$ and PTE are almost the same as the system in the completely aligned state. At this time, the ferrite cores in the coil

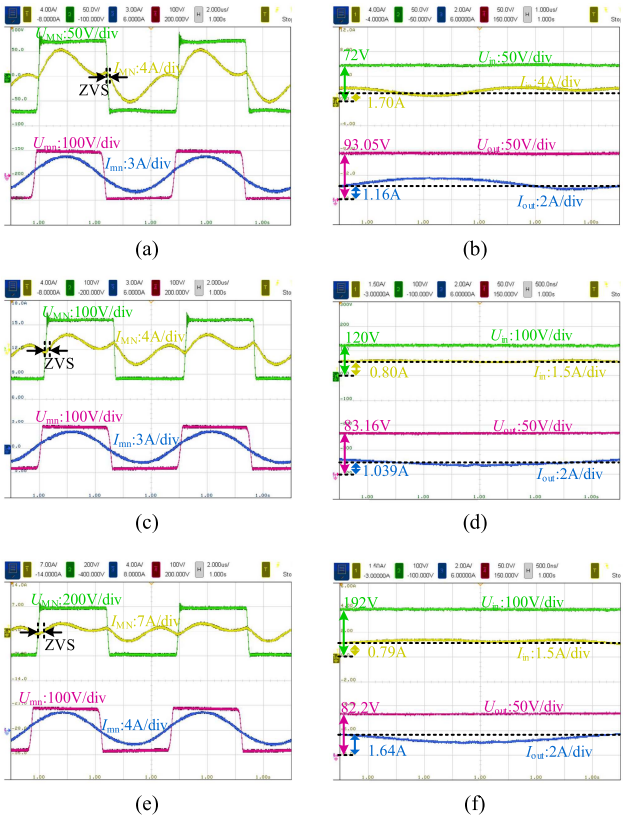

Fig. 20. Waveform diagram of BAPV-IPT system under different winding taps. (a) Tap-1, $R = 80\ \Omega$, AC side. (b) Tap-1, $R = 80\ \Omega$, DC side. (c) Tap-2, $R = 80\ \Omega$, AC side. (d) Tap-2, $R = 80\ \Omega$, DC side. (e) Tap-3, $R = 50\ \Omega$, AC side. (f) Tap-3, $R = 50\ \Omega$, DC side.

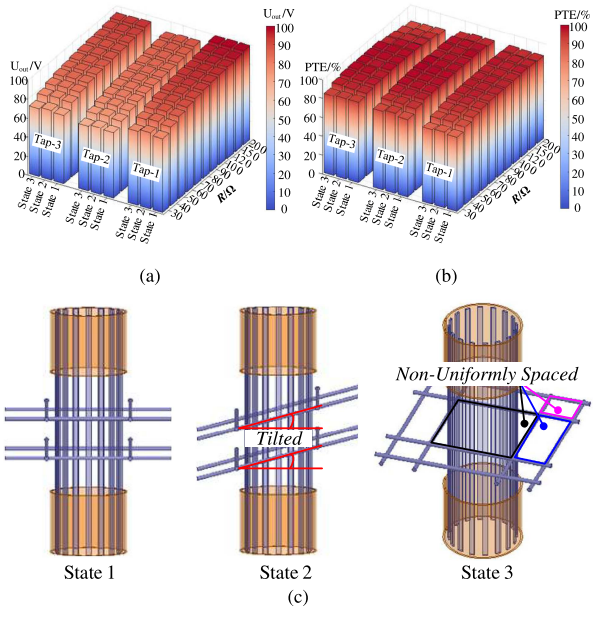

Fig. 21. Output characteristics of the proposed BAPV-IPT system under different rebar configurations. (a) Output voltage U_{out}. (b) PTE. (c) Rebar configuration states.

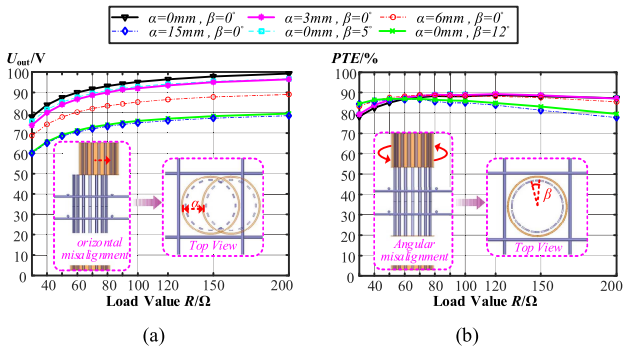

Fig. 22. Output characteristics of BAPV-IPT system under horizontal and angular misalignment of coil. (a) Output voltage U_{out}. (b) PTE.

are all in contact with FB. Magnetic flux can propagate between the transmitting and the receiving stage along the consecutive magnetic cores. When α increases to 6 mm, several ferrite cores within the coil become disconnected from the FB. The mutual inductance between the transmitting and receiving coils is reduced to a small range and the voltage gain of the IPT system is changed. U_{out} is reduced by about 10 V, and PTE is highly consistent with the alignment state. When $\alpha = 15$ mm and $\beta = 12°$, none of the ferrite cores in the coil remain in contact with the FB. The magnetic flux is transferred from the coil to FB through the air gap. As a result, the magnetic coupling between the transmitting and receiving stages is significantly weakened, and the voltage gain is further diminished. Since the proposed system has parameter reconfigurable features, the voltage deviation can be compensated by switching the winding taps. In addition, PTE performs well under heavy load conditions, and decreases slightly under light load but still exceeds 80%.

The tolerance of the BAPV-IPT system to coil misalignment can be further improved by increasing the number of ferrite cores. However, this will generate more core losses. In addition, the incremental increase in the coupling coefficient contributed by additional ferrite cores beyond sixteen is marginal. The improvement in system efficiency is disproportionate to the associated increase in cost. Therefore, the number of ferrite cores should not be increased indiscriminately.

A comprehensive comparison of the proposed reconfigurable BAPV-IPT system with similar works from recent years is presented in Table IV. Compared with the BAPV and IPT systems proposed in work [22], power transfer across reinforced concrete walls is achieved. The transmission distance is greatly increased by FB, and the PTE of the IPT system is further improved. Compared with the works in [25], [26], and [27], the proposed system uses significantly fewer coils. In addition, the transmission performance of the IPT system is comprehensively and effectively enhanced in this work. The power transfer scheme to overcome the reinforced concrete wall is extended from the SHM system to the BAPV system. Moreover, the PV output fluctuation is effectively limited by the proposed parameter reconfigurable scheme. As a result, the operational stability of the BAPV-IPT system is significantly improved. In addition, for the BAPV scenario, the proposed parameter reconfiguration scheme offers

advantages over conventional converter regulation methods. The additional energy conversion stage and the use of complex driver circuits are avoided in this work, resulting in a simpler control strategy and a more flexible design process.

V. Conclusion

A WPT solution for the BAPV system is proposed in this article. The coupling coefficient is significantly enhanced by the proposed FB. The photovoltaic power generation components are wirelessly connected to the indoor microgrid through the FB embedded in the wall. The adverse effects of rebars on the IPT system are analyzed through FEM and significantly reduced by electrical insulation. A multitap autocoupling magnetic structure based on CSC is proposed. The voltage conversion ratio of the IPT system is tunable by switching the winding taps on the primary side. By switching the winding taps, the system effectively compensates for output voltage fluctuations caused by changes in solar irradiance. The circuit model of the BAPV-IPT system is established, the PTE of the equivalent T^2 circuit and the losses in each part of the system are analyzed. Among them, the core loss is measured and verified by a large signal characterization method. A prototype of a three-tap IPT system is built and experiments are conducted across a 360-mm simulated wall. Multiple sets of experiments under different tap states and input powers are completed. The system can achieve efficiencies of about 90% with power levels of several hundred watts.

References

[1] M. Sechilariu, B. Wang, and F. Locment, "Building integrated photovoltaic system with energy storage and smart grid communication," *IEEE Trans. Ind. Electron.*, vol. 60, no. 4, pp. 1607–1618, Apr. 2013.

[2] V. Poulek, M.-Q. Dang, M. Libra, V. Beránek, and J. Safránková, "PV panel with integrated lithium accumulators for BAPV applications—One year thermal evaluation," *IEEE J. Photovolt.*, vol. 10, no. 1, pp. 150–152, Jan. 2020.

[3] A. Demetriou, D. Buxton, and C. A. Charalambous, "Stray current DC corrosion blind spots inherent to large PV systems fault detection mechanisms: Elaboration of a novel concept," *IEEE Trans. Power Del.*, vol. 33, no. 1, pp. 3–11, Feb. 2018.

[4] M. A. Quintana, D. L. King, T. J. McMahon, and C. R. Osterwald, "Commonly observed degradation in field-aged photovoltaic modules," in *Proc. Conf. Rec. 29th IEEE Photovolt. Specialists Conf.*, 2002, pp. 1436–1439.

[5] B. Minnaert, S. Ravyts, J. Driesen, and N. Stevens, "Challenges for wireless power transfer in building-integrated photovoltaics," in *Proc. IEEE PELS Workshop Emerg. Technol., Wireless Power Transfer*, 2018, pp. 1–5.

[6] Y. Zhang et al., "An integrated electric vehicle charging system of wireless power transfer and auxiliary power module with shared converter and magnetic coupler," *IEEE Trans. Ind. Electron.*, vol. 71, no. 9, pp. 10414–10421, Sep. 2024.

[7] Y. Wang, T. Li, M. Zeng, J. Mai, P. Gu, and D. Xu, "An underwater simultaneous wireless power and data transfer system for AUV with high-rate full-duplex communication," *IEEE Trans. Power Electron.*, vol. 38, no. 1, pp. 619–633, Jan. 2023.

[8] Z. Li, J. He, Y. Huo, M. Ban, Y. Liu, and J. Liu, "High-misalignment tolerance and output adjustable wireless charging system via detuned series–Series compensated reconfigurable transmission channels," *IEEE Trans. Power Electron.*, vol. 38, no. 10, pp. 11786–11801, Oct. 2023.

[9] H. Zhang, Z. Li, and C.-K. Lee, "Transmitter adaptation and wireless power control for capsule endoscopy," *IEEE Trans. Power Electron.*, vol. 39, no. 4, pp. 4884–4894, Apr. 2024.

[10] Q. Wang et al., "Inductive power transfer system with constant current-constant voltage charging tolerating misalignment based on multiobjective optimization for compensation topology," *IEEE Trans. Power Electron.*, vol. 40, no. 3, pp. 4581–4591, Mar. 2025.

[11] X. Qu, W. Zhang, S.-C. Wong, and C. K. Tse, "Design of a current-source-output inductive power transfer LED lighting system," *IEEE J. Emerg. Sel. Top. Power Electron.*, vol. 3, no. 1, pp. 306–314, Mar. 2015.

[12] Q. Deng et al., "Frequency-dependent resistance of litz-wire square solenoid coils and quality factor optimization for wireless power transfer," *IEEE Trans. Ind. Electron.*, vol. 63, no. 5, pp. 2825–2837, May 2016.

[13] J. Deng, W. Li, T. D. Nguyen, S. Li, and C. C. Mi, "Compact and efficient bipolar coupler for wireless power chargers: Design and analysis," *IEEE Trans. Power Electron.*, vol. 30, no. 11, pp. 6130–6140, Nov. 2015.

[14] B. H. Choi, V. X. Thai, E. S. Lee, J. H. Kim, and C. T. Rim, "Dipole-coil-based wide-range inductive power transfer systems for wireless sensors," *IEEE Trans. Ind. Electron.*, vol. 63, no. 5, pp. 3158–3167, May 2016.

[15] C. Park, S. Lee, G.-H. Cho, and C. T. Rim, "Innovative 5-m-off-distance inductive power transfer systems with optimally shaped dipole coils," *IEEE Trans. Power Electron.*, vol. 30, no. 2, pp. 817–827, Feb. 2015.

[16] P. Gu et al., "A three-stage-five-coil IPT system based on cylindrical solenoid coupler applied to State detection equipment of HV device," *IEEE Trans. Power Electron.*, vol. 37, no. 2, pp. 2382–2393, Feb. 2022.

[17] P. Gu, D. Yang, G. Li, B. Zhou, F. Wei, and H. Guan, "Analysis and design of discrete ferrite rings to improve the efficiency of meter-range wireless gap inductive power transfer system," *IEEE Trans. Power Electron.*, vol. 38, no. 10, pp. 11802–11813, Oct. 2023.

[18] D. Wang, F. Chen, J. Zhang, S. Cui, Z. Bie, and C. Zhu, "A novel pendulum-type magnetic coupler with high misalignment tolerance for AUV underwater wireless power transfer systems," *IEEE Trans. Power Electron.*, vol. 38, no. 12, pp. 14861–14871, Dec. 2023.

[19] Y. Wang, P. Gu, Y. Yao, and D. Xu, "Analysis and design of cubic magnetic coupler for high distance-to-diameter ratio IPT systems," *IEEE Trans. Ind. Electron.*, vol. 69, no. 1, pp. 409–419, Jan. 2022.

[20] P. K. Chittoor and B. Chokkalingam, "Wireless electrification system for photovoltaic powered autonomous drone charging," *IEEE Trans. Transp. Electrific.*, vol. 10, no. 2, pp. 3002–3011, Jun. 2024.

[21] P. K. Chittoor and B. Chokkalingam, "Building integrated photovoltaic powered wireless drone charging system," *Sol. Energy*, vol. 252, no. 1, pp. 163–175, Mar. 2023.

[22] H. Wang, J. Sun, and K. W. E. Cheng, "A compact and integrated magnetic coupler design with cross-coupling elimination utilizing LCC-S compensation network for building attached photovoltaic systems," *IEEE Trans. Magn.*, vol. 59, no. 11, Nov. 2023, Art. no. 8401205.

[23] S.-H. Lee, M.-Y. Kim, B.-S. Lee, and J. Lee, "Impact of rebar and concrete on power dissipation of wireless power transfer systems," *IEEE Trans. Ind. Electron.*, vol. 67, no. 1, pp. 276–287, Jan. 2020.

[24] Y. Peng, W. Qi, Y. Chen, R. Mai, and U. K. Madawala, "Wireless sensor power supply based on eddy currents for structural health monitoring," *IEEE Trans. Ind. Electron.*, vol. 71, no. 7, pp. 7252–7261, Jul. 2024.

[25] L. Qian, K. Cui, H. Xia, H. Shao, J. Wang, and Y. Xia, "An inductive power transfer system for powering wireless sensor nodes in structural health monitoring applications," *IEEE Trans. Microw. Theory Techn.*, vol. 70, no. 7, pp. 3732–3740, Jul. 2022.

[26] Y. Jang, J.-K. Han, J.-I. Baek, G.-W. Moon, J.-M. Kim, and H. Sohn, "Novel multi-coil resonator design for wireless power transfer through reinforced concrete structure with rebar array," in *Proc. IEEE 3rd Int. Future Energy Electron. Conf. ECCE Asia*, 2017, pp. 2238–2243.

[27] Y. Peng, E. Ma, Q. Wang, Y. Chen, R. Mai, and U. K. Madawala, "Maximizing output power of inductive power transfer systems under rebar array shielding," *IEEE Trans. Power Electron.*, vol. 39, no. 10, pp. 13934–13945, Oct. 2024.

[28] G. Velasco-Quesada, M. Roman-Lumbreras, and A. Conesa-Roca, "Comparison of central dimmer systems based on multiple-tapped autotransformer and high-frequency switching converter," *IEEE Trans. Ind. Electron.*, vol. 59, no. 4, pp. 1841–1848, Apr. 2012.

[29] A. K. Adapa and V. John, "Active-phase converter for operation of three-phase induction motors on single-phase grid," *IEEE Trans. Ind. Appl.*, vol. 53, no. 6, pp. 5668–5675, Nov./Dec. 2017.

[30] C. Li and J. A. Cobos, "A switched capacitor and autotransformer hybrid converter with DC current in the windings," *IEEE Trans. Power Electron.*, vol. 37, no. 2, pp. 1870–1884, Feb. 2022.

[31] W. Lin, J. Wen, and S. Cheng, "Multiport DC–DC autotransformer for interconnecting multiple high-voltage DC systems at low cost," *IEEE Trans. Power Electron.*, vol. 30, no. 12, pp. 6648–6660, Dec. 2015.

[32] R. Abdollahi, G. B. Gharehpetian, A. Anvari-Moghaddam, and F. Blaabjerg, "A 40-pulse autotransformer rectifier based on new pulse multiplication circuit for aviation application," *IEEE Trans. Ind. Electron.*, vol. 70, no. 11, pp. 10822–10832, Nov. 2023.

[33] R. Abdollahi and G. B. Gharehpetian, "Inclusive design and implementation of novel 40-pulse AC–DC converter for retrofit applications and harmonic mitigation," *IEEE Trans. Ind. Electron.*, vol. 63, no. 2, pp. 667–677, Feb. 2016.
[34] A. Ghosh, A. Ukil, and A. P. Hu, "Integration of rooftop solar PV generation with wireless power transfer," in *Proc. IEEE PES Asia-Pacific Power Energy Eng. Conf.*, 2019, pp. 1–5.
[35] I.-W. Iam, C.-K. Choi, C.-S. Lam, P.-I. Mak, and R. P. Martins, "A constant-power and optimal-transfer-efficiency wireless inductive power transfer converter for battery charger," *IEEE Trans. Ind. Electron.*, vol. 71, no. 1, pp. 450–461, Jan. 2024.
[36] C. Cai et al., "Robust wide-area wireless charging of multipath movable receivers: A coupling mechanism and simplified configuration strategy," *IEEE Trans. Power Electron.*, vol. 40, no. 1, pp. 2527–2541, Jan. 2025.
[37] C. Jiang, X. Li, S. S. Ghosh, H. Zhao, Y. Shen, and T. Long, "Nanocrystalline powder cores for high-power high-frequency power electronics applications," *IEEE Trans. Power Electron.*, vol. 35, no. 10, pp. 10821–10830, Oct. 2020.
[38] Z. Luo, X. Li, C. Jiang, Z. Li, and T. Long, "Permeability-adjustable nanocrystalline flake ribbon in customized high-frequency magnetic components," *IEEE Trans. Power Electron.*, vol. 39, no. 3, pp. 3477–3485, Mar. 2024.

Peng Gu (Member, IEEE) was born in Harbin, Heilongjiang Province, China. He received the B.S. degree from Huazhong University of Science and Technology (HUST), Wuhan, China, in 2015, the M.S. degree from China Electric Power Research Institute (CEPRI), Beijing, China, in 2018, and the Ph.D. degree from Harbin Institute of Technology (HIT), Harbin, China, in 2023, all in electrical engineering.

He has been working as a Faculty Member with Northeastern University (NEU), Shenyang, China, in electrical engineering, since 2023. He has also been working as a Postdoctoral Fellow with NEU in control science and engineering, since 2023. His current research interests include wireless power transfer, magnetic coupling structure design, power system analysis, electromagnetic transient analysis, and dc–dc converter.

Dr. Gu was the recipient of the 2024 IEEE Transactions on Power Electronics First Place Prize Paper Award. He was the recipient of the Outstanding Ph.D. Thesis Award from HIT, in 2023, and from China Energy Research Society (CERS), in 2024.

Xingzhen Guo was born in Shandong Province, China, in 2002. He received the B.S. degree in electrical engineering and automation from Heilongjiang University, Harbin, China, in 2024. He is currently working toward the M.S. degree in electrical engineering from the College of Information Science and Engineering, Northeastern University, Shenyang, China.

His research interests include wireless power transfer and magnetic coupling structure design.

Yunrui Hao was born in Hebei Province, China, in 1999. He received the B.S. degree in industrial engineering, in 2022, from Northeastern University, Shenyang, China, where he is currently working toward the M.S degree.

His research interests include wireless power transfer and fault diagnosis.

Xinzhe Wang (Graduate Student Member, IEEE) was born in Anhui Province, China, in 2003. He received the B.S. degree in electrical engineering and automation from Anhui University of Technology, China, in 2025. He is currently working toward the M.S. degree in electrical engineering from the College of Information Science and Engineering, Northeastern University, Shenyang, China.

His research interests include wireless power transfer and magnetic coupling structure design.

Jiliang Zhang (Senior Member, IEEE) received the B.E., M.E., and Ph.D. degrees in information and communication engineering from Harbin Institute of Technology, Harbin, China, in 2007, 2009, and 2014, respectively.

He was an Associate Professor with the School of Information Science and Engineering, Lanzhou University, from 2017 to 2019, a Researcher with the Department of Electrical Engineering, Chalmers University of Technology, Sweden, from 2017 to 2018, a Marie Curie Research Fellow and a KTP Associate with the Department of Electronic and Electrical Engineering, The University of Sheffield, U.K., from 2018 to 2022. He is currently a Full Professor with the College of Information Science and Engineering, Northeastern University. He has pioneered systematic building wireless performance evaluation, modeling, and optimization, with the key concepts summarized in Fundamental Wireless Performance of a Building, IEEE Wireless Communications, 29(1), 2022. His research interests include, but are not limited to, wireless channel modeling, modulation system, relay system, vehicular communications, ultra-dense small cell networks, and smart environment modeling.

Dongsheng Yang (Senior Member, IEEE) received the B.S. degree in testing technology and instrumentation, the M.S. degree in power electronics and electric drives, and the Ph.D. degree in control theory and control engineering from Northeastern University, Shenyang, China, in 1999, 2004, and 2007, respectively.

He is currently a Professor with Northeastern University. He was supported by the Program for New Century Excellent Talents in University. He has authored or coauthored more than 70 papers published in academic journals and conference proceedings, three monographs, and coinvented 80 patents. His current research interests include distributed generation, wireless power transfer, multienergy power system, and artificial intelligence-based fault diagnosis and protection.

Dr. Yang was a recipient of the Second Prize of National Science and Technology Progress.

Yijie Wang (Senior Member, IEEE) was born in Heilongjiang Province, China, in 1982. He received the B.S., M.S., and Ph.D. degrees in electrical engineering from Harbin Institute of Technology, Harbin, China, in 2005, 2007, and 2012, respectively.

From 2012 to 2014, he was a Lecturer with the Department of Electrical and Electronics Engineering, Harbin Institute of Technology. From 2014 to 2017, he was an Associate Professor with the Department of Electrical and Electronics Engineering, Harbin Institute of Technology. Since 2017, he has been a Professor with the Department of Electrical and Electronics Engineering, Harbin Institute of Technology. His research interests include wireless power transfer, dc–dc converters, soft-switching power converters, power factor correction circuits, digital control electronic ballasts, and LED lighting systems.

Dr. Wang is an Associate Editor of IEEE TRANSACTIONS ON INDUSTRIAL ELECTRONICS, IEEE JOURNAL OF EMERGING AND SELECTED TOPICS IN POWER ELECTRONICS, IEEE ACCESS, IET POWER ELECTRONICS, and *Journal of Power Electronics*.